Jinst

Published by IOP Publishing for Sissa Medialab

Received: *March 15, 2021*
Revised: *May 24, 2021*
Accepted: *July 3, 2021*
Published: *August 12, 2021*

# On the space resolution of the μ-RWELL

**G. Bencivenni,**[a] **C. Capoccia,**[a] **G. Cibinetto,**[b] **R. de Oliveira,**[c] **R. Farinelli,**[b] **G. Felici,**[a] **M. Gatta,**[a] **M. Giovannetti,**[a,d,*] **L. Lavezzi,**[e,f] **G. Morello,**[a] **M. Poli Lener**[a] **and E. Tskhadadze**[a,g]

[a] *INFN, Laboratori Nazionali di Frascati, Via Enrico Fermi 54, 00044 Frascati (Roma), Italy*
[b] *INFN, Sezione di Ferrara, Via Saragat 1, 44122 Ferrara, Italy*
[c] *CERN, Esplanade des Particules 1, 1217 Meyrin, Switzerland*
[d] *Department of Physics, University of Rome "Tor Vergata", Via della Ricerca Scientifica 1, 00133 Rome, Italy*
[e] *Department of Physics, University of Torino, Via P. Giuria 1, 10125 Torino, Italy*
[f] *INFN, Sezione di Torino, Via P. Giuria 1, 10125 Torino, Italy*
[g] *Tbilisi State University, 1 Ilia Tchavtchavadze Avenue, 0179 Tbilisi, Georgia*

*E-mail:* matteo.giovannetti@lnf.infn.it

Abstract: In micro-pattern gaseous detectors (MPGD) the evaluation of the space resolution with the charge centroid method provides large uncertainty when the incident particle is not perpendicular to the readout plane. An improvement of the position reconstruction is given by the microTPC (μTPC) algorithm: the three-dimensional reconstruction of the particle track inside the detector drift gap is performed using the arrival time of the induced signals on the readout. In this work we report the application of this method to the μ-RWELL detector that, combined with the charge centroid, allows to achieve an almost uniform resolution below 100 μm over a wide angular range.

Keywords: Micropattern gaseous detectors (MSGC, GEM, THGEM, RETHGEM, MHSP, MICROPIC, MICROMEGAS, InGrid, etc); Particle tracking detectors (Gaseous detectors); Gaseous detectors; Time projection Chambers (TPC)

*Corresponding author.



https://doi.org/10.1088/1748-0221/16/08/P08036

2021 JINST 16 P08036

## Contents



2021 JINST 16 P08036

## 1 Introduction

The μ-RWELL is a single-amplification stage resistive MPGD [1] composed of two elements, figure 1: the cathode, a simple PCB with a thin copper layer on one side and the μ-RWELL_PCB, the core of the detector. The baseline version of the μ-RWELL_PCB is a multi-layer circuit realized by means of standard photo-lithography technology. It is composed of three layers: a well patterned single copper-clad polyimide (Apical®) foil[1] acting as amplification element of the detector; a resistive layer realized with a Diamond-Like-Carbon (DLC) film sputtered on the bottom side of the polyimide foil working as discharge limitation stage; a standard PCB for readout purposes, segmented as strip, pixel or pad electrodes.

Applying a suitable voltage between the copper layer and the DLC, the well acts as a multiplication channel for the ionization produced in the drift gas gap, figure 2. Besides the suppression of the streamer-to-discharge transition, with a mechanism similar to the one of the Resistive Plate Counters (RPC, [3–6]), the presence of the DLC affects the rate capability [7] and the space resolution [8] of the detector. In particular, concerning the effects on the space resolution, the charge induced on the resistive film is spread with a time constant [8, 9] that depends on the surface resistivity (in the following simply called resistivity) and the capacitance per unit area between the resistive layer and the readout plane.[2] As shown in [8], the best space resolution (∼50 μm) with a strip-pitch of 400 μm and particles crossing the detector perpendicular with respect to the readout plane, has been achieved with a DLC resistivity around 100 MΩ/□, using the classical charge centroid (CC) method for the position reconstruction.

[1] 50 μm thick polyimide covered on one side with 5 μm thick copper, similar to the GEM [2] base material.

[2] The time constant is $\tau = \rho c = \rho\epsilon_0\epsilon_r/t$ in wich $\rho$ is the resistivity, $c$ the capacitance and $t$ the distance between the DLC and the readout.

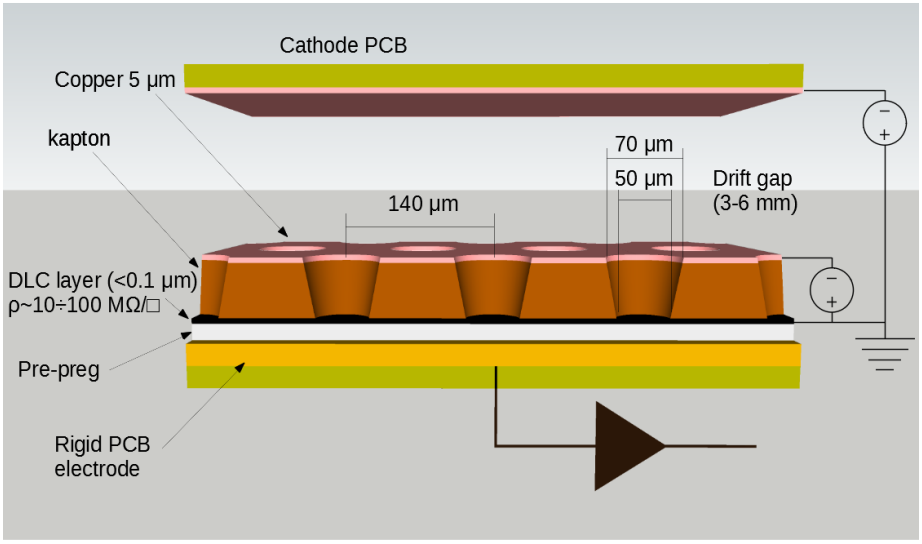


**Figure 1.** Baseline layout of the μ-RWELL.

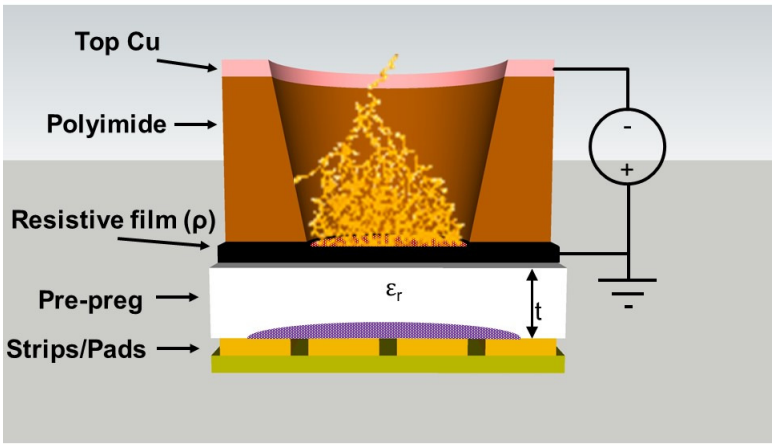


**Figure 2.** Principle of operation of the μ-RWELL detector.

The purpose of this paper is to investigate the space resolution of a μ-RWELL exposed to a particle beam crossing the detector with an angle ranging from 0° to 45° with respect to the perpendicular to the readout plane. In the next sections we describe the experimental setup, the description of the two position reconstruction analysis methods, concluding with the discussion of the beam test results.



2021 JINST 16 P08036

## 2 Experimental setup

The test was performed at the H8-SPS beam area at CERN with a 150 GeV/c muon beam and the setup is shown in figure 3. Two μ-RWELLs have been installed on different plates that have been rotated with the same angle with respect to the beam direction. Two GEM detectors equipped with a two-dimensional strip readout have been used as external trackers in order to clean the data sample[3] and four plastic scintillators have been used as trigger.

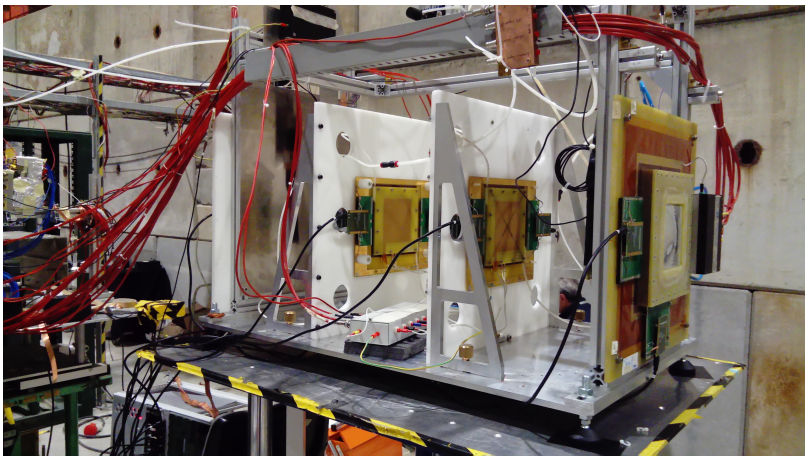

**Figure 3.** Experimental setup: all the detectors have a $10 \times 10$ cm$^2$ active area. The distance between the two μ-RWELL detectors is 30 cm.

The μ-RWELLs used (figure 4) are derived from the Double Resistive Layer (DRL) layout [7]: two metallic vias matrices connect two resistive stages to the readout plane for the grounding, with a vias density of 1 cm$^{-2}$. The first stage is a DLC layer, while the second is made of ~5 mm long resistors screen-printed on a polyimide substrate. The μ-RWELLs, flushed with an Ar:$CO_2$:$CF_4$ = 45:15:40 gas mixture, have been operated at a gain of 5000. They have been equipped with a 400 μm pitch strip-segmented PCB read out with APV25 front-end electronics (FEE) [10]. The 6 mm large drift gap, allowing the formation of a large number of primary ionization clusters, is an important requirement for the μTPC method. The detectors have been tested at different drift fields ($E_D$) in the range 0.5 ÷ 3 kV/cm.

## 3 The charge centroid and the μTPC reconstruction methods

For a detector equipped with a strip-segmented readout and instrumented with analog FEE, when a set of contiguous strips is fired the charge centroid position of the track can be computed as

$$x_{CC} = \frac{\sum x_k q_k}{\sum q_k}, \tag{3.1}$$

where $x_k$ and $q_k$ are respectively the coordinate and the charge induced on the $k$-th strip. The uncertainty associated to $x_{CC}$ is expected to increase with the impinging angle of the track (θ in figure 5). To overcome this issue an alternative approach has been recently proposed.

[3]The trackers have been also used to estimate the beam divergence: ~ 1°.



2021 JINST 16 P08036

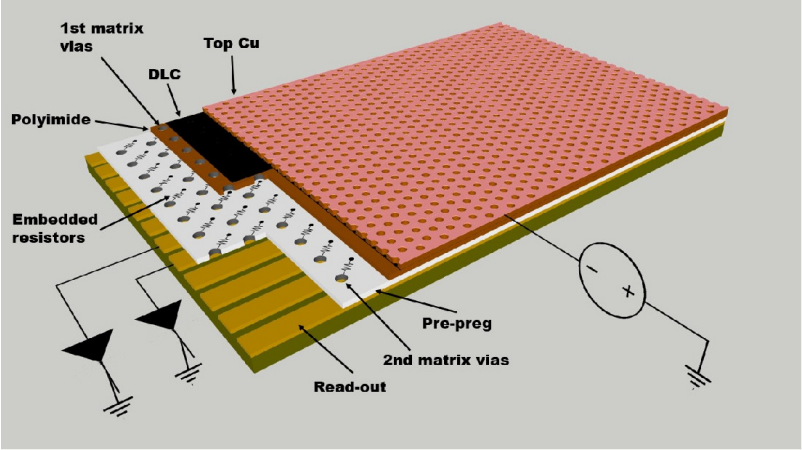


**Figure 4.** Sketch of the Double Resistive Layer μ-RWELL with embedded resistors.

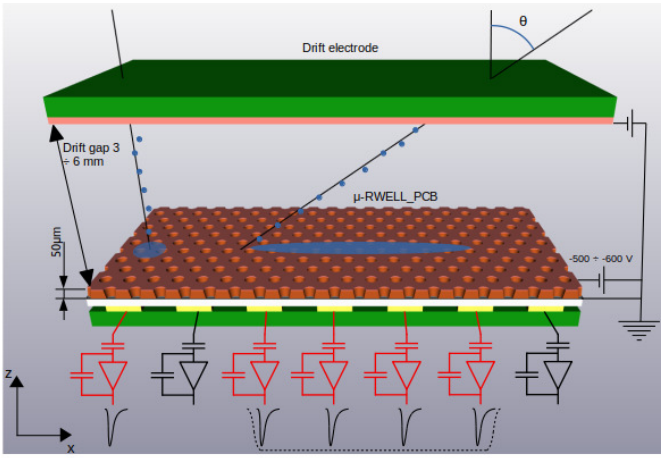


**Figure 5.** A simplified sketch showing how a non orthogonal track affects the number of fired strips.

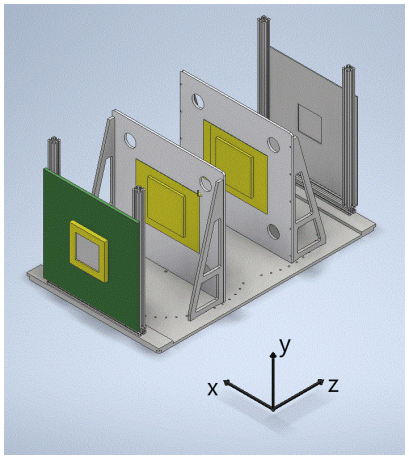


**Figure 6.** Sketch of the experimental setup with the coordinate system.

The idea of the μTPC method, developed for the MicroMegas of the ATLAS New Small Wheels [11, 12] and successively implemented by other collaborations [13–15], is to reconstruct a track segment inside the detector drift gap rather than using only its projection on the readout plane. The procedure, inspired to the Time Projection Chamber (TPC) concept [16, 17] is based on the measurement of both charge and arrival time of the signal collected on the readout strips. The electrons, created by an ionizing particle crossing the drift gap, move towards the amplification region in a given time. By the measurement of the electrons arrival time on each strip and the knowledge of the drift velocity in the gas mixture, the position of the ionization clusters can be localized in the drift gap. A linear fit to these clusters provides a three-dimensional reconstruction of the track. In our case the readout is segmented in one-dimensional strips parallel to the $y$ axis, so that only a reconstruction in what we define the $x-z$ plane (figures 5, 6) is available. For each cluster $k$, the hits on the strips are recorded at different times $t_k$, depending on the distance of the ionization



2021 JINST 16 P08036

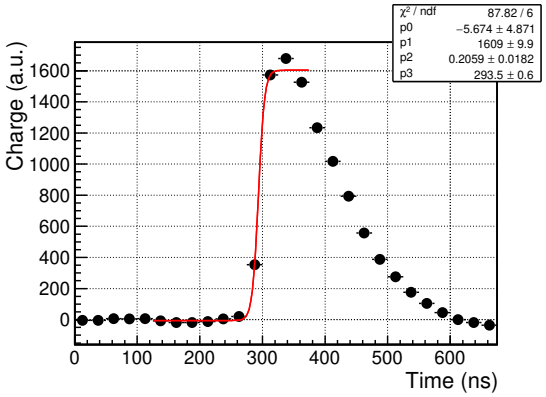


**Figure 7.** Charge signal as a function of the sampling time fitted with a Fermi-Dirac function: $Q = p_0 + p_1/(1 + \exp(p_2 \cdot (p_3 - x)))$.

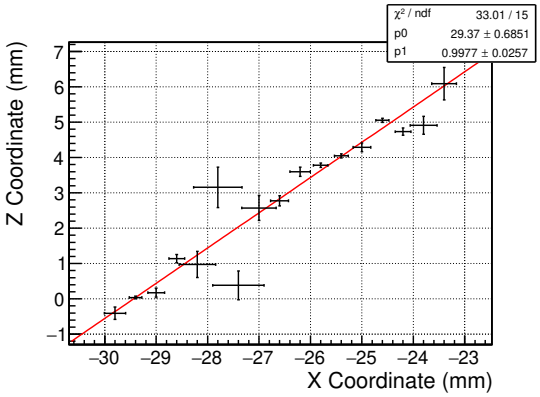


**Figure 8.** Example of a 45° track segment as reconstructed using the μTPC algorithm with the linear fit: $z = p_0 + p_1 \cdot x$. The smaller the charge collected on a strip, the larger the $x$ coordinate error.

electrons from the readout plane.[4] Each $t_k$ is evaluated by fitting the leading edge of the charge signal with a Fermi-Dirac function and taking its flex point, figure 7. The $x_k$ coordinate is given by the centre of each fired strip while the $z_k$ coordinate by the time measurement using the formula:

$$z_k = v_{\text{drift}} \cdot (t_k - t_0) \tag{3.2}$$

where $v_{\text{drift}}$ is the electron drift velocity in the gas and $t_0$ is the common trigger time given by the scintillators. In the formula 3.2, thanks to the good uniformity of the drift field in MPGDs, the velocity of the electrons can be considered constant. The drift velocity at different drift fields is computed with MAGBOLTZ [18], a tool included in GARFIELD simulation program [19]. Figure 8 shows the track segment reconstruction of an event using this algorithm. The error bars on the $x$ axis account for the strip pitch and the charge collected on the strip. The error bars on the $z$ axis depend on the drift velocity and the error on $t_k$.[5] Another possible choice for the reconstructed point errors, taking into account diffusion effects, is stated in [12]. Following the approach of other authors [12, 14, 15], the intersection of the linear fit of the track segment with the middle of the drift gap is taken as the coordinate associated with the track. This is useful for all the applications requiring only a coordinate and not the complete track segment.

## 4 Beam test results

The space resolution of a single detector is extracted from the width of the residuals distribution ($\sigma_{\text{res}}$), defined as the difference between the coordinates associated with the track as reconstructed by

[4] In the APV25 the charge of the signal is sampled in 25 ns time bins. For measurements described in this paper the sampling is asynchronous with respect to the trigger from scintillators. This results in a 25 ns time jitter.

[5] $\Delta z_k = \Delta t_k \cdot v_d$, where $\Delta t_k$ is the error from the Fermi-Dirac fit. $\Delta^2 x_k = \left(\frac{\text{pitch}}{\sqrt{12}}\right)^2 + \left(\frac{\text{pitch}}{\sqrt{12}} \cdot \frac{\langle q \rangle}{q_k}\right)^2$, where $q_k$ is the charge induced on the $k$-th strip and $\langle q \rangle$ is the average charge of the clusters for the event. The latter has been adopted from [14] signed by some of the co-authors of this paper.



2021 JINST 16 P08036

the two μ-RWELLs.[6] This choice allows its evaluation without the need of the track reconstruction by external trackers. Assuming the same contribution for each μ-RWELL, the space resolution of the single device is obtained as $\sigma_x = \sigma_{res}/\sqrt{2}$. For sake of simplicity in this paper all the plots show the residuals scaled by a factor of $1/\sqrt{2}$ in order to directly provide the detector space resolution. The residuals are studied for both CC and μTPC methods. The data set has been cleaned requiring a full reconstruction (x-view and y-view) from the two trackers. All the data reported have been taken inside a fiducial area to avoid edge effects. A cut of 50 ADC counts has been chosen on each FEE channel. The cluster has been defined as a collection of contiguous fired strips, with no more than one skipped strip inside. In case of multiple clusters, the one with the largest charge has been chosen. For the CC method the minimum cluster size required is 1 while for the μTPC is 2, thus leading to a difference of total events between the two selections less than 2%. All these cuts reject no more than the 15% of the total events.

In order to take into account the presence of the tails in the residuals distribution, we fit the data with the linear combination of two Gaussian curves, eq. (4.1), in which $\mu_{1,2}$ and $\sigma_{1,2}$ are their mean value and standard deviation. The width of the residuals distribution ($\sigma_x$) is defined as the standard deviation of $f(x)$, eq. (4.2). This is a slightly different approach with respect to the analysis reported in [12]. A comparison between the two methods is shown in appendix A.

$$f(x) = Ae^{-\frac{1}{2}\left(\frac{x-\mu_1}{\sigma_1}\right)^2} + Be^{-\frac{1}{2}\left(\frac{x-\mu_2}{\sigma_2}\right)^2} \tag{4.1}$$

$$\sigma_x = \frac{1}{(A\sigma_1 + B\sigma_2)}\sqrt{A^2\sigma_1^4 + B^2\sigma_2^4 + AB\sigma_1\sigma_2\left((\mu_1-\mu_2)^2 + \sigma_1^2 + \sigma_2^2\right)} \tag{4.2}$$

In figure 9a the residuals distribution is shown, suggesting the presence of systematic effects typically due to geometrical distortions of the detectors or misalignment of the setup. As a consequence the residuals exhibit a non constant behaviour as a function of data parameters, such as the $x_{CC}$ and $x_{TPC}$ coordinate, the parameters $p_0$ and $p_1$ from the μTPC linear fit or the parameters from the trackers fit. In order to correct these effects, for each dependence we have first parameterized the residuals profile by a suitable polynomial function and then, event by event, we have applied the correction. In the following the correction of the residuals distribution, reconstructed with the μTPC algorithm, as a function of the $x$ coordinate, is shown as an example of this procedure. Plotting the residuals as a function of the μTPC-reconstructed $x$ coordinate, figure 9b, a clear dependence is visible, suggesting a rototraslation of the setup due to mechanical tolerance of the support. By means of a fifth order polynomial fit of the profile, the residuals are corrected obtaining an almost flat graph centred around zero, figures 9c, 9d. As an example of the contribution of the main dependencies, the resolution obtained during the sequence of corrections are reported in table 1 for two data sets.

The residuals distribution after all the corrections is shown in figure 10. The space resolution has been evaluated at different θ using both CC and μTPC methods. As expected the CC provides the best result for orthogonal tracks while increasing the angle the resolution quickly gets worse, figure 11a. On the contrary the μTPC shows a better behaviour for large angles, figure 11b: the longer the projected track segment on the readout plane the larger the number of points to be

[6]The 25 ns time jitter from the APV adds a global offset to the reconstructed track. Such an offset can be cancelled if the differences between the two chamber (having the same jitter) is considere to evaluate the spatial resolution.



2021 JINST 16 P08036

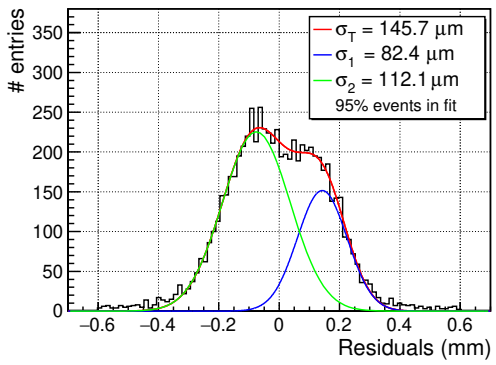


**(a)** Residuals distribution before any correction.

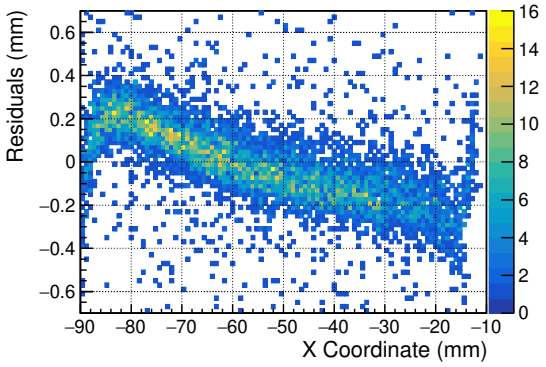


**(b)** Residuals as a function of the $x$ coordinate before the correction.

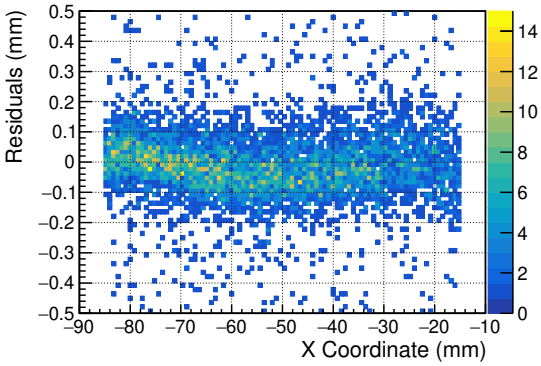


**(c)** Residuals as a function of the $x$ coordinate after the correction.

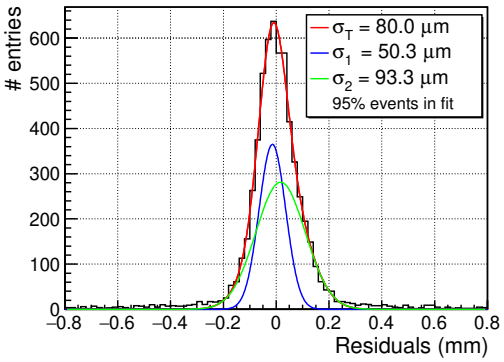


**(d)** Residuals distribution after the $x$ coordinate correction.

**Figure 9.** µTPC reconstruction, for $E_D$ = 1 kV/cm, and θ = 30°: dependence of the residuals distribution on the $x$ coordinate reconstructed in one of the two chambers. A fiducial zone, $x > -82$ mm and $x < -22$ mm, has been taken into account in order to avoid edge effects.

**Table 1.** Space resolutions after correcting the main dependencies of the residuals on the reconstruction parameters, for two data sets with $E_D$ = 1kV/cm.

| | 0° CC [µm] | 30°µTPC [µm] |
|---|---|---|
| No corrections | 102 | 146 |
| $x$ coordinate | 85 | 80 |
| Angular coefficients from trackers fit | 78 | 79 |
| Angular coefficients from µTPC fit ($p_1$) | | 76 |
| Mean $z$ coordinate of the reconstructed clusters | | 72 |
| Constant terms from trackers fit | 73 | 70 |

2021 JINST 16 P08036

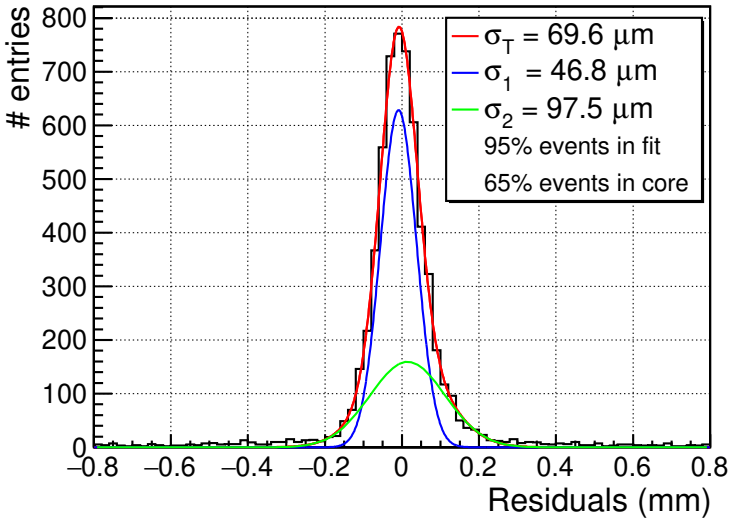


**Figure 10.** μTPC reconstruction, $E_D$ = 1 kV/cm, θ = 30°: residuals distribution after all the dependencies corrections.

fitted. Since the μTPC method depends on the drift velocity of the electrons in the gas mixture, and consequently on the drift field, a study at different drift fields has been performed, figure 11b. For our gas mixture the electron drift velocity increases with the drift field in the range 0.5÷3 kV/cm [20]. The lower the drift velocity the smaller the uncertainty on the reconstruction of the $z$ coordinate, improving the μTPC fit, eq. (3.2).

In order to improve the reconstruction accuracy, we have chosen to combine the two measurements, event by event, with the following weighted average:

$$x_{\text{comb}} = \frac{x_{\text{CC}}/\sigma^2_{\text{CC}} + x_{\text{TPC}}/\sigma^2_{\text{TPC}}}{1/\sigma^2_{\text{CC}} + 1/\sigma^2_{\text{TPC}}}, \tag{4.3}$$

where $x_{\text{CC}}$ and $x_{\text{TPC}}$ are the already corrected coordinates reconstructed with the two methods and $\sigma_{\text{CC}}$ e $\sigma_{\text{TPC}}$ are the corresponding resolutions at a given angle θ.

The combined space resolution is thus obtained from the fit of the $x_{\text{comb}}$ residuals distribution with equation (4.1).

In figure 12 the resolutions for both CC and the μTPC are compared and displayed along with the combined resolution from eq. (4.3). The combination of the two algorithms results in a space resolutions below 100 μm for the whole angular range.

## 5 Conclusions

The μTPC method has been successfully implemented for the reconstruction of the track segment in a μ-RWELL, studying the performances by varying the electric field in the drift gas gap. Combining the μTPC algorithm with the charge centroid an almost uniform space resolution over a wide range of track incidence angles is obtained. At low drift fields the measured space resolution improves reaching values down to 65 μm.



2021 JINST 16 P08036

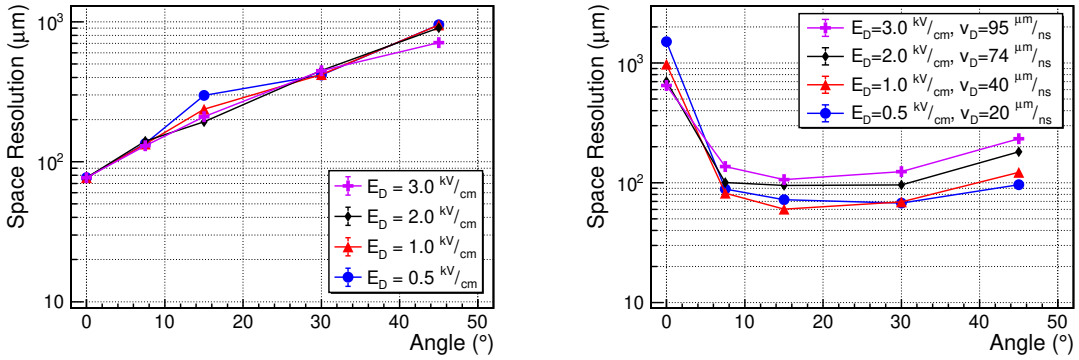


**(a)** CC space resolution.

**(b)** μTPC space resolution.

**Figure 11.** The results of the two reconstruction algorithms, over a large angular range, for various drift field values.

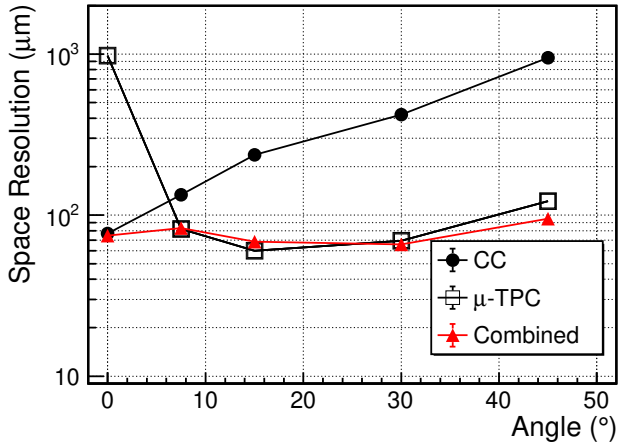


**Figure 12.** Comparison of the two algorithms with their combined reconstruction, at a drift field $E_D$=1 kV/cm.

## A Consideration upon the double Gaussian fit

As previously stated, equations. (4.1) and (4.2) were used to estimate the space resolution of the μ-RWELL detectors. There is not an univocal approach to this task, for example in [12] the width of the residuals distribution, fitted with the same function (4.1), was defined as [21][7]

$$\sigma^2 = \frac{V_1\sigma_1^2 + V_2\sigma_2^2}{V_1 + V_2}, \tag{A.1}$$

in which $V_{1,2}$ are the integrals of the two Gaussian functions: $V_1 = \sqrt{2\pi}A\sigma_1$ and $V_2 = \sqrt{2\pi}B\sigma_2$. The equation (4.2) reduces to (A.1) only if the two Gaussian curves have the same mean, $\mu_1 = \mu_2$, namely for a symmetric residuals distribution. The proof follows straightforward (adding and

[7] Author of [12].



2021 JINST 16 P08036

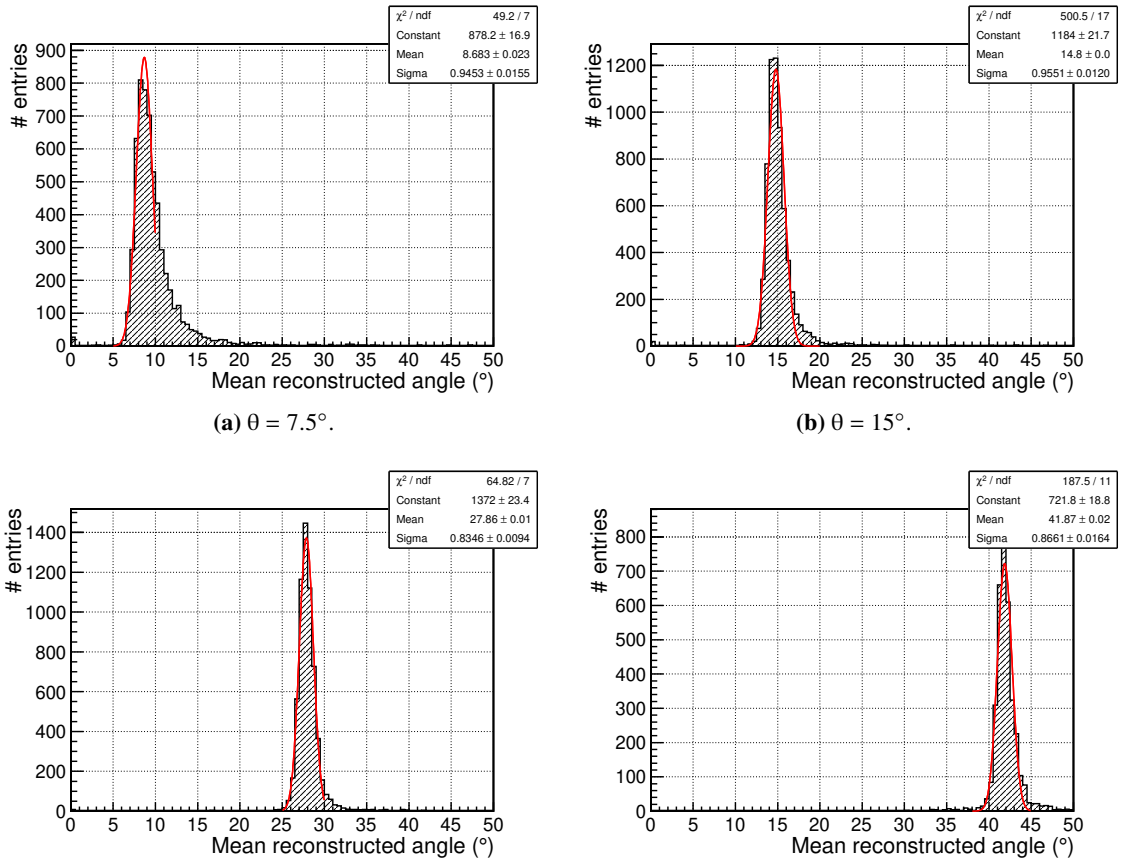


**(a)** θ = 7.5°.

**(b)** θ = 15°.

**(c)** θ = 30°.

**(d)** θ = 45°.

**Figure 13.** Distributions of the reconstructed angles for different configurations.

subtracting the term $2AB\sigma_1^2\sigma_2^2$ from eq. (4.2)):

$$\begin{aligned}\sigma_x^2 &= \frac{A^2\sigma_1^4 + B^2\sigma_2^4 + AB\sigma_1\sigma_2\left(\sigma_1^2+\sigma_2^2\right) + 2AB\sigma_1^2\sigma_2^2 - 2AB\sigma_1^2\sigma_2^2}{(A\sigma_1 + B\sigma_2)^2} \\ &= \frac{(A\sigma_1^2 + B\sigma_2^2)^2 + AB\sigma_1\sigma_2(\sigma_1-\sigma_2)^2}{(A\sigma_1+B\sigma_2)^2} = \frac{(V_1\sigma_1 + V_2\sigma_2)^2 + V_1V_2(\sigma_1-\sigma_2)^2}{(V_1+V_2)^2} \\ &= \frac{(V_1^2+V_1V_2)\sigma_1^2 + (V_2^2+V_1V_2)\sigma_2^2}{(V_1+V_2)^2} = \frac{V_1\cancel{(V_1+V_2)}\sigma_1^2 + V_2\cancel{(V_1+V_2)}\sigma_2^2}{(V_1+V_2)\cancel{^2}} = \sigma^2\end{aligned} \tag{A.2}$$

## B Angle reconstruction from the μTPC fit

The incidence angle of the track could be evaluated from the angular coefficient of the μTPC linear fit inside the gas gap. A gaussian fit for the reconstructed angles has been done, figures 13. For the 7.5° data set the fit interval has been shrinked due to the presence of an asymmetric tail. Figure 14 points out how the μTPC fails with orthogonal tracks. In figure 15 are reported the gaussian fit parameters.



2021 JINST 16 P08036

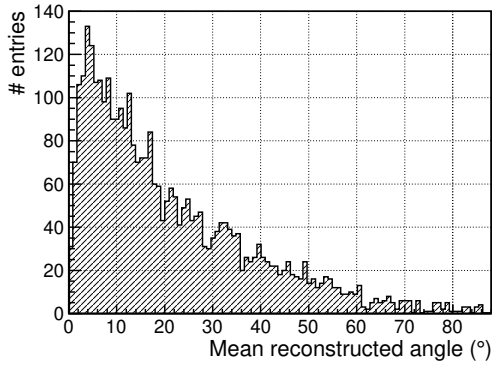


**Figure 14.** Distribution of the reconstructed angles for the case of perpendicular impinging particles, $\theta = 0°$.

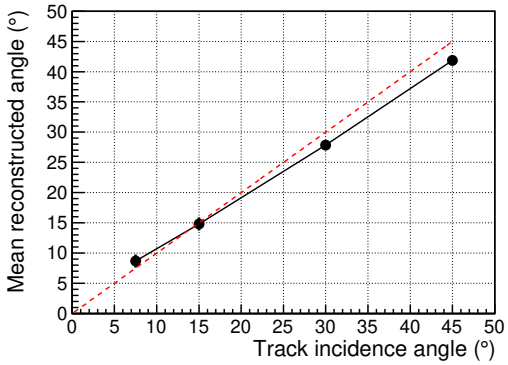


**Figure 15.** Mean value from the fit of the reconstructed angle as a function of the true angle (dotted line as a reference). The error bars ($\sigma$) are smaller than the markers.

## References


[1] G. Bencivenni, R. De Oliveira, G. Morello and M.P. Lener, *The μ-resistive WELL detector: a compact spark-protected single amplification-stage MPGD*, 2015 *JINST* **10** P02008 [arXiv:1411.2466].

[2] F. Sauli, *GEM: a new concept for electron amplification in gas detectors*, *Nucl. Instrum. Meth. A* **386** (1997) 531.

[3] V. Parkhomchuck, Y. Pestov and N. Petrovykh, *A spark counter with large area*, *Nucl. Instrum. Meth.* **93** (1971) 269.

[4] R. Santonico and R. Cardarelli, *Development of resistive plate counters*, *Nucl. Instrum. Meth.* **187** (1981) 377.

[5] M. Anelli, G. Bencivenni, G. Felici and L. Magro, *Glass electrode spark counters*, *Nucl. Instrum. Meth. A* **300** (1991) 572.

[6] P. Fonte et al., *Advances in the development of micropattern gaseous detectors with resistive electrodes*, *Nucl. Instrum. Meth. A* **661** (2012) S153 [arXiv:1005.1477].

[7] G. Bencivenni et al., *The μ-RWELL layouts for high particle rate*, 2019 *JINST* **14** P05014 [arXiv:1903.11017].

[8] G. Bencivenni et al., *Performance of μ-RWELL detector vs. resistivity of the resistive stage*, *Nucl. Instrum. Meth. A* **886** (2018) 36.

[9] M.S. Dixit and A. Rankin, *Simulating the charge dispersion phenomena in micro pattern gas detectors with a resistive anode*, *Nucl. Instrum. Meth. A* **566** (2006) 281 [physics/0605121].

[10] M. Raymond et al., *The APV25 0.25 μm CMOS readout chip for the CMS tracker*, *IEEE Nucl. Sci. Symp. Conf. Rec.* **2** (2000) 9/113.

[11] T. Alexopoulos et al., *Development of large size MicrOMEGAs detector for the upgrade of the ATLAS muon system*, *Nucl. Instrum. Meth. A* **617** (2010) 161.

[12] T. Alexopoulos et al., *Performance studies of resistive-strip bulk MicrOMEGAs detectors in view of the ATLAS new small wheel upgrade*, *Nucl. Instrum. Meth. A* **937** (2019) 125.


2021 JINST 16 P08036

[13] D. Pfeiffer et al., *The μTPC method: improving the position resolution of neutron detectors based on MPGDs*, 2015 *JINST* **10** P04004 [arXiv:1501.05022].

[14] M. Alexeev et al., *Triple GEM performance in magnetic field*, 2019 *JINST* **14** P08018 [arXiv:1908.06253].

[15] A. Amoroso et al., *Time performance of a triple-GEM detector at high rate*, 2020 *JINST* **15** P06013 [arXiv:2004.04944].

[16] D.R. Nygren, *Proposal to investigate the feasibility of a novel concept in particle detection*, Lawrence Berkeley National Laboratory internal report, Berkeley, CA, U.S.A. (1974).

[17] J.N. Marx and D.R. Nygren, *The time projection chamber*, *Phys. Today* **31N10** (1978) 46.

[18] S. Biagi, *Magboltz — transport of electrons in gas mixtures webpage*, http://magboltz.web.cern.ch/magboltz/.

[19] R. Veenhof, *Garfield — simulation of gaseous detectors webpage*, http://garfield.web.cern.ch/garfield/.

[20] M. Alfonsi et al., *High-rate particle triggering with triple-GEM detector*, *Nucl. Instrum. Meth. A* **518** (2004) 106.

[21] M. Iodice, private communication.

2021 JINST 16 P08036